

**Review: MR Physics for Clinicians****Physics of MRI: A Primer****CME**Donald B. Plewes, PhD<sup>1\*</sup> and Walter Kucharczyk, MD<sup>2</sup>

This article is accredited as a journal-based CME activity. If you wish to receive credit for this activity, please refer to the website: [www.wileyblackwellcme.com](http://www.wileyblackwellcme.com)

**ACCREDITATION AND DESIGNATION STATEMENT**

Blackwell Futura Media Services designates this journal-based CME activity for a maximum of 1 *AMA PRA Category 1 Credit*<sup>TM</sup>. Physicians should only claim credit commensurate with the extent of their participation in the activity.

Blackwell Futura Media Services is accredited by the Accreditation Council for Continuing Medical Education to provide continuing medical education for physicians.

**EDUCATIONAL OBJECTIVES**

Upon completion of this educational activity, participants will be better able to discuss how magnetic field gradients are used to facilitate spatial encoding.

**ACTIVITY DISCLOSURES**

No commercial support has been accepted related to the development or publication of this activity.

**Faculty Disclosures:**

The following contributors have no conflicts of interest to disclose:

Editor-in-Chief: C. Leon Partain, MD, PhD

CME Editor: Scott B. Reeder, MD, PhD

CME Committee: Scott Nagle, MD, PhD, Pratik Mukherjee, MD, PhD, Shreyas Vasanaawala, MD, PhD, Bonnie Joe, MD, PhD, Tim Leiner, MD, PhD, Sabine Weckbach, MD, Frank Korosec, PhD

Authors: Donald B. Plewes, PhD, Walter Kucharczyk, MD

This manuscript underwent peer review in line with the standards of editorial integrity and publication ethics maintained by *Journal of Magnetic Resonance Imaging*. The peer reviewers have no relevant financial relationships. The

peer review process for *Journal of Magnetic Resonance Imaging* is double-blinded. As such, the identities of the reviewers are not disclosed in line with the standard accepted practices of medical journal peer review.

Conflicts of interest have been identified and resolved in accordance with Blackwell Futura Media Services's Policy on Activity Disclosure and Conflict of Interest. No relevant financial relationships exist for any individual in control of the content and therefore there were no conflicts to resolve.

**INSTRUCTIONS ON RECEIVING CREDIT**

For information on applicability and acceptance of CME credit for this activity, please consult your professional licensing board.

This activity is designed to be completed within an hour; physicians should claim only those credits that reflect the time actually spent in the activity. To successfully earn credit, participants must complete the activity during the valid credit period.

Follow these steps to earn credit:

- Log on to [www.wileyblackwellcme.com](http://www.wileyblackwellcme.com)
- Read the target audience, educational objectives, and activity disclosures.
- Read the article in print or online format.
- Reflect on the article.
- Access the CME Exam, and choose the best answer to each question.
- Complete the required evaluation component of the activity.

This activity will be available for CME credit for twelve months following its publication date. At that time, it will be reviewed and potentially updated and extended for an additional period.

<sup>1</sup>Department of Medical Biophysics, University of Toronto, Toronto, Ontario, Canada.

<sup>2</sup>Department of Medical Imaging, University of Toronto, Toronto, Ontario, Canada.

\*Address reprint requests to: D.B.P., Sunnybrook Health Sciences Centre Imaging Research – S651, 2075 Bayview Ave., Toronto, Ontario, Canada, M4N-3M5. E-mail: [don.plewes@sunnybrook.ca](mailto:don.plewes@sunnybrook.ca)

Received August 3, 2011; Accepted February 15, 2012.

DOI 10.1002/jmri.23642

View this article online at [wileyonlinelibrary.com](http://wileyonlinelibrary.com).

This article is based on an introductory lecture given for the past many years during the "MR Physics and Techniques for Clinicians" course at the Annual Meeting of the ISMRM. This introduction is not intended to be a comprehensive overview of the field, as the subject of magnetic resonance imaging (MRI) physics is large and complex. Rather, it is intended to lay a conceptual foundation by which magnetic resonance image formation can be understood from an intuitive perspective. The presentation is nonmathematical, relying on simple models that take the reader progressively from the basic *spin* physics of nuclei, through descriptions of how the magnetic resonance signal is generated and detected in an MRI scanner, the foundations of nuclear magnetic resonance (NMR) relaxation, and a discussion of the Fourier transform and its relation to MR image formation. The article continues with a discussion of how magnetic field gradients are used to facilitate spatial encoding and concludes with a development of basic pulse sequences and the factors defining image contrast.

**Key Words:** MRI physics; *k*-space; NMR relaxation; MRI image formation

**J. Magn. Reson. Imaging 2012;35:1038–1054.**

© 2012 Wiley Periodicals, Inc.

WITHOUT QUESTION, magnetic resonance imaging (MRI) is one of the wonders of modern medicine. It is a remarkable imaging technology, which offers exquisite soft tissue contrast of high spatial resolution, with a tomographic 3D presentation and the capability of demonstrating dynamic physiologic changes. Through various alterations of how MR images are acquired, one can generate images that report an enormous array of physical/physiologic phenomena based on the rich physics of nuclear magnetic resonance (NMR). Images can be created with contrast reflecting proton density, T1 and T2 relaxation times (1), tissue susceptibility variations (2,3), diffusion (4–6), temperature (7), fields of motion (8–11), biomechanical properties (12–14), tissue perfusion (15–17), electrical currents (18), oxygen levels (19–21), and spectra of key biochemical species (22–25), to mention only a few. Furthermore, MRI does all of this in a non-invasive manner, which permits safe repeated scans with no known harm (26) when used within well-defined technical constraints (27). Over its short history, since the original studies by Lauterbur (28) and Mansfield and colleagues (29,30) and similar formative studies that quickly followed thereafter (31–37), MRI has become a central pillar to much of modern medical practice. However, the principles of MRI are

subtle and less intuitively apparent in comparison to more traditional medical imaging such as radiography, computed tomography (CT), positron emission tomography (PET), or ultrasound. To appreciate its subtleties and understand its limitations, one requires a joint understanding of the basic physics of NMR and the mathematics of the Fourier transform, both of which can be challenging. As such, it is the aim of this review article to provide a primer on the very basic physics of MRI that can be used as a foundation to approach more challenging contemporary MRI literature. It is aimed at physicians and technologists who seek to gain an intuitive understanding of the nature of the MRI signals, the factors that influence them, and how these signals are gathered to form the beautiful MRI images to which we have become accustomed. Necessarily, this article will be cursory, as the subject of MRI is large and growing, but will build a conceptual foundation on which the broad sweep of modern MRI techniques and its uses can be understood.

#### WHAT MAKES THE MRI SIGNAL?

MRI is founded on the basic physics of NMR, which was first experimentally demonstrated in 1946 independently by Purcell et al (38) and Bloch (39). The key ingredient that enables NMR is the existence of a curious property of many subatomic particles known as *spin*. Not all nuclei exhibit spin, which is restricted to those with an odd number of neutrons or protons (40). For example,  $^{12}\text{C}$  has six protons and six neutrons and exhibits no spin. However, the isotope of carbon  $^{13}\text{C}$ , which exists with a natural abundance of 1.1%, is composed of seven neutrons and six protons and results in a net spin. In the case of MRI, the majority of imaging that is performed today is based on the nucleus of hydrogen or the single proton, which also exhibits a spin. Table 1 shows a list of several isotopes that are relevant to MRI including hydrogen, sodium, and phosphorous, which are all present in nearly 100% abundance and have spin; however, the concentration of these nuclei in tissues varies from 88 Molar for protons to millimolar concentrations for  $^{23}\text{Na}$  and  $^{31}\text{P}$  (41). While images can be made with each of these nuclei, the time required gathering images with useful spatial resolution and image quality can vary by orders of magnitude, with protons requiring the least time due in part to its high concentration in vivo in the form of water.

Table 1  
NMR Properties of Various Isotopes

Nucleus	Spin (42)	Gyromagnetic ratio (MHz/T) (42)	Natural abundance (42)	Concentration in human tissue (41)
Hydrogen $^1\text{H}$	1/2	42.58	~100%	88M
Deuterium $^2\text{H}$	1	6.53	0.015%	13 mM
Sodium $^{23}\text{Na}$	3/2	11.27	~100%	80 mM
Phosphorous $^{31}\text{P}$	1/2	1.131	~100%	75 mM
Oxygen $^{17}\text{O}$	5/2	-5.77	0.04%	16 mM
Fluorine $^{19}\text{F}$	1/2	2.627	~100%	4 mM

In the second column, it is noted that the spin of these different nuclei show fractional values and are expressed in units of Planck's constant. This is a measure of the *angular momentum* of the nucleus, which is a feature of rotating objects to continue in their rotation unless disturbed. Angular momentum is the rotational version of the more familiar notion of translational momentum in which a moving object continues in its state of linear motion unless it is resisted by some force. For example, a molecule can exhibit angular momentum due to its history and environment. However, theory and early experiments showed that the angular momentum is found to be quantized in discrete levels measured in units of Planck's constant defined by an integer quantum number  $J$ . In this case, the measured angular momentum could range from  $-J, -J+1, \dots, 0, 1, 2, \dots, J$  in units of Planck's constant. However, when the angular momenta of electrons or protons were measured, it was found that they also demonstrated discrete values separated by units of  $h$  but that any measurement was found to be either  $+h/2$  or  $-h/2$  but not zero (42). The notion of a half integer spin posed a severe challenge for the physics community in the 1920s through 1930s and spans a fascinating period in the progress of modern physics. It became clear that the existence of this half integer angular momentum cannot arise from something that was actually spinning (42), but rather was something intrinsic to the particle itself, much like its mass or charge. This intrinsic property is known as *spin* and is listed in the second column of Table 1. The history of our understanding of spin is one of the most profound achievements of early 20th century physics. It is a remarkable story of experimental skill (43) and theoretical insight (44), mixed with some measure of good fortune and daring guesswork (45). Those interested in learning more of this extraordinary history are encouraged to turn to a number of entertaining and very accessible historical accounts (46–48).

While the notion of spin is fundamentally a quantum mechanical concept, it is fortunate that when studying many (although not all) of the basic concepts as applied to proton MRI, the need to take a strictly quantum perspective can be relaxed and one can safely resort to a more traditional "classical" perspective to gain a functional understanding of the principles of MRI. This in conjunction with a judicious choice of quantum mechanical concepts provides a reasonable base from which to appreciate the main principles of MRI.

Consider Fig. 1, where a proton is portrayed as a spinning sphere with charge and mass. The spin of the proton, seen as a rotation of the nucleus about some axis, in conjunction with its charge, gives the proton a magnetic property similar to a small bar magnet. If this magnetic structure were placed in an applied magnetic field  $B_0$ , it would tend to align with that field, as shown in Fig. 1a. However, in addition to its magnetic property, spin gives the proton angular momentum (as already discussed). The significance of this feature is best understood by drawing an analogy with a hanging gyroscope, as shown in Fig. 1b. If that

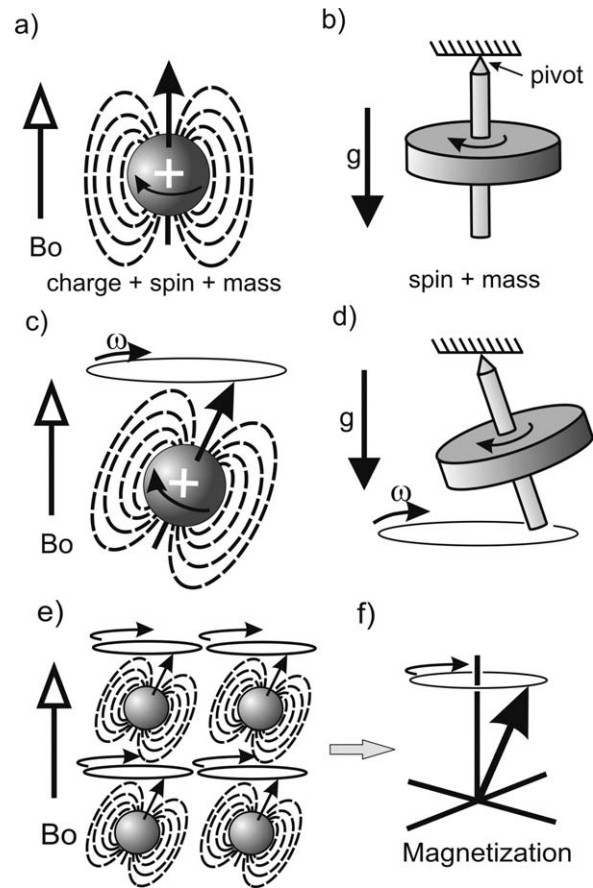


**Figure 1.** The spin and charge of a proton (a) causes it to have a magnetic field that tends to align with an applied magnetic field  $B_0$  analogous to a gyroscope hanging from a vertical pivot in the earth's gravitational field (b). When the gyroscope is tilted away from vertical it undergoes precession (d). Similarly, the proton also has angular momentum in the form of spin, which will cause it to precess at a frequency  $\omega$  when it is tipped out of alignment with the  $B_0$  field (c). A group of spins precess in synchrony when exposed to a uniform magnetic field (e), which forms a bulk magnetization (f) represented by a vector that precesses at the same frequency.

gyroscope were left undisturbed, it would naturally align vertically, parallel to the direction of its own weight in the earth's gravitational field (g). However, if the gyroscope was disturbed, by tipping it out of this vertical alignment, upon release the gyroscope would wobble or "precess" about the vertical axis, as indicated in Fig. 1d. This curious motion is a result of the combined effect of the torque that the gyroscope experiences from its weight and its angular momentum due to its rotation. In comparison to a proton, it has already been pointed out that it exhibits quantized angular momentum due to its spin and is magnetic due to the combined effect of spin and charge. As such, if the spin were tipped from its natural alignment with the applied magnetic field, it would precess about the direction of the applied magnet field  $B_0$ , as shown in Fig. 1c. In the case of the gyroscope, its precessional frequency,  $\omega$ , is dictated by the strength of the gravitation field and the mass, geometry, and

rotation rate of the gyroscope. In a similar manner, the proton's precessional frequency, known as the Larmor frequency ( $\omega$ ), is dictated by the strength of the applied magnetic field  $B_0$  through a constant  $\gamma$  known as the gyromagnetic ratio, which factors the nuclear details into a single number. The key point is that the precession frequency is given by  $\gamma \cdot B_0$ , the product of the applied field and gyromagnetic ratio. For example, at a field strength of 1 Tesla ( $\approx 20,000$  times larger than the earth's surface magnetic field), the proton Larmor frequency is 42.57 Mhz. Doubling the magnetic field to 2 T will increase the Larmor frequency to 85.14 MHZ. In Table 1, the gyromagnetic ratio of many nuclei has been summarized, which in turn shows that the proton has the highest Larmor frequency among this list.

**DETECTING AND EXCITING IN NMR**

In tissue, the concentration of protons is enormous and, as such, one would expect a large magnetic effect from these aligned protons. However, the number of protons that ultimately contribute to the NMR signal is much smaller than that suggested by its tissue density, with only  $\approx 1$  in 100,000 protons actually contributing to the final NMR signal at magnetic fields of 1.5 T at body temperature. In the absence of a magnetic field, nuclei with  $\frac{1}{2}$  spin are equally distributed between two states, thus canceling their collective magnetic effect. However, when exposed to a magnetic field the population of spins that are parallel to the applied field become slightly more probable than those that are opposed. It is this slight imbalance that generates a bulk magnetic effect. It is these excess protons that are sketched in Fig. 1e. As they experience the same magnetic field, they precess in synchrony to coherently contribute to a tissue "bulk magnetization," which can be represented as a single vector that precesses about the magnetic field  $B_0$  (Fig. 1f).

In order to detect this precessing magnetization, a pair of receiver coils are frequently used, as shown in Fig. 2a. These are connected to sensitive amplifiers that are tuned to the Larmor frequency. The time-varying magnetic field from the rotating magnetization will induce a tiny signal in the coils, which oscillates at the Larmor frequency. Only the time-varying part of the magnetization is capable of inducing a signal in the coil and as such only the rotating component of the magnetization in the x-y plane is detected. This time-varying component of the magnetization is referred to as the "transverse" component as opposed to the "longitudinal" component, which is parallel to the  $B_0$  field. The axis of each coil is aligned to the transverse plane so that the changing magnetic field of the transverse component can couple with each coil and induce a signal. The size of the signal is a result of magnetic induction, which in turn is proportional to the rate of change of the magnetization present at the coil. By using two coils it is possible to determine the direction of rotation of the magnetization as well as the angle of the transverse magnetization at any

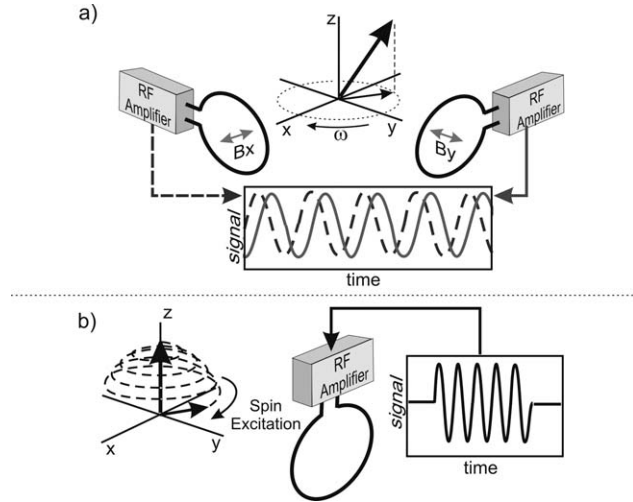


**Figure 2.** Rotating magnetization induces a signal that oscillates at frequency  $\omega$  via an amplified tuned coil. Two coils placed a right angles sample different phases of the rotating magnetization (a) which can be used to measure the spin phase. Transverse magnetization can be generated by an applied alternating magnetic field at frequency  $\omega$  causing the magnetization to nutate away from the Z axis toward the transverse plane (b).

time. This can be appreciated by noting that the phase of the signals represented by the dashed and solid lines is shifted by  $90^\circ$ . By considering the ratio of the signals, it is possible to determine the angle of the rotating transverse magnetization as a function of time with respect to the transverse coordinates. This feature will be mentioned below (Measuring the k-Space Amplitude/Phase), where the use of the MRI signal for image formation is discussed.

As mentioned above, the equilibrium bulk magnetization is aligned parallel to the  $B_0$  field (along the Z-axis) if left undisturbed. Thus as there is no component of the magnetization in the transverse plane, it cannot precess and generate a signal. In order to generate an NMR signal, the magnetization must be tipped away from this equilibrium alignment so that a component of the magnetization lies in the transverse plane where it is free to precess. To achieve this, the spins are exposed to an alternating magnetic field (Fig. 2b), which is referred to as the B1 field and must have a frequency equal to the Larmor frequency of the nucleus. In this figure, only one coil is shown, although two coils can also be used for excitation where the signals to the coils are shifted by  $90^\circ$ , similar to that of detection shown in Fig. 2a. This form of quadrature transmit coil arrangement permits a more efficient use of RF energy to achieve the desired excitation as compared to a single transmit coil.

As the Larmor frequencies are typically in the MHz range, which corresponds to the "radiofrequency" range of the electromagnetic spectrum, these pulses are referred to as radiofrequency or "RF" pulses. Again, geometry is important and the B1 field is most effective when it lies in the transverse plane and perpendicular to the  $B_0$  field. By virtue of this alternating applied magnetic field, the spins can progressively

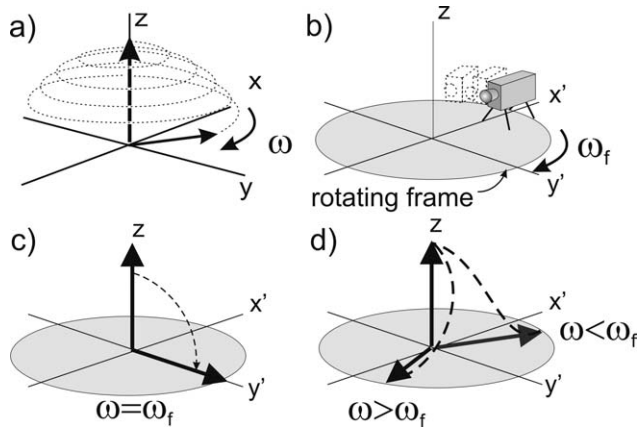


**Figure 3.** The excitation of magnetization as viewed from a stationary frame of reference (a). A rotating frame of reference revolves about the stationary frame at frequency  $\omega_f$  (b). Excitation as viewed from the rotating frame of reference when  $\omega_f$  matches (c) and does not match (d) the proton Larmor frequency.

absorb energy and nutate away from the longitudinal axis to create the time-varying transverse component. The angle through which the magnetization undergoes nutation depends on both the amplitude of the RF field and its duration. By careful choice of these two parameters, the magnetization can be tipped to any orientation relative to the Z-axis.

If the frequency of the B1 field is not equal to the Larmor frequency, it will not cause the magnetization to rotate away from the longitudinal axis. It would be natural at this point to ask how close the two frequencies must be in order to excite the nuclei into precession. The answer to this question is somewhat complex and depends on the transverse relaxation time constant, which will be described in subsequent sections. This transverse relaxation time defines the spread of frequencies that can initiate excitation such that the shorter the relaxation time, the greater the spread. In practical terms, this range of frequencies for most tissues encountered in standard MRI can vary from  $\approx 1$ –100 Hz, depending on the tissue in question.

### ROTATING FRAME OF REFERENCE

The motion of the magnetization vector during excitation is complex, as it simultaneously nutates away from the Z-axis and undergoes precession in the transverse plane at the Larmor frequency (Fig. 3a). In order to simplify this complex motion, it is helpful to view the spin system from a special frame of reference, which itself rotates about the Z-axis. To appreciate this concept, consider a turntable that revolves about the Z-axis at a frequency  $\omega_f$ , which carries a small camera (Fig. 3b). If the frequency of the rotating frame is matched to the Larmor frequency, the magnetization, the turntable, and the camera are all seen rotating about the Z-axis in synchrony. If the magnetization vector is viewed through the rotating camera, the magnetization vector slowly nutates from the Z-

axis toward the y-axis without any precession in the transverse plane (Fig. 3c). From this new point of view, it is apparent that the motion of magnetization can be simplified so that its precession is eliminated and only nutation remains. However, if the Larmor frequency ( $\omega$ ) is slightly lower or higher than the frequency of the rotating frame of reference ( $\omega_f$ ), the magnetization will precess in the rotating frame at a frequency that corresponds to the difference between the Larmor frequency and that of the rotating frame, as seen in Fig. 3d. Thus, the magnetization can appear to precess in either direction with a frequency dictated by this frequency difference.

### SPIN DEPHASING AND TRANSVERSE RELAXATION

Up to this point, an assumption has been made that the magnetic field applied to the magnetization is spatially homogeneous. However, even with an ideal magnet capable of an absolutely uniform magnetic field, the introduction of tissue into the field can result in subtle changes in the spatial distribution of the magnetic field, depending on the tissue itself. This means that magnetization residing in tissue with its unavoidable heterogeneity will experience slightly different fields and thus precess at different Larmor frequencies (Fig. 4a). As viewed from the rotating frame with a frequency set at a rotation rate equal to the average frequency of the spin ensemble, the magnetization vectors will gradually fan out in the transverse plane (Fig. 4b), progressively losing their alignment. Since the magnetization is the vector sum of the individual contribution of the spins, this vector sum will tend toward zero and exhibit a drop in signal with time (Fig. 4c). This is referred to as “relaxation” and is characterized by the time needed to reduce the signal to  $1/e$  or 37% of its maximum value.

At this point, it would be reasonable to question what mechanism causes the spins to experience

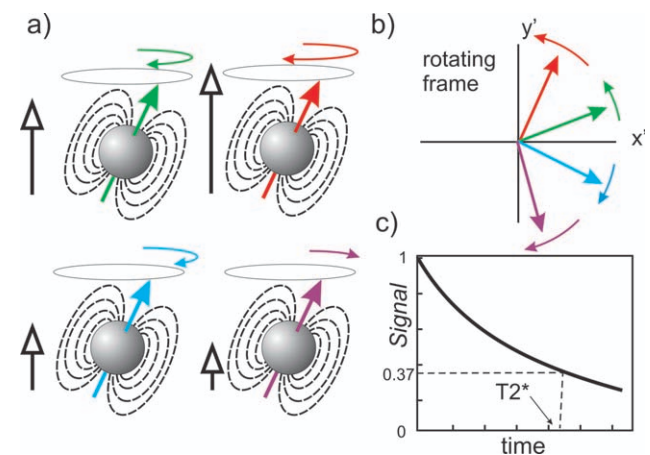


**Figure 4.** The dephasing of magnetization arising from variations in the static magnetic field throughout the tissue (a). The components of transverse magnetization accumulate an increasing range of phase with time (b) causing a progressive signal loss, which is characterized by the decay time constant  $T2^*$  (c).

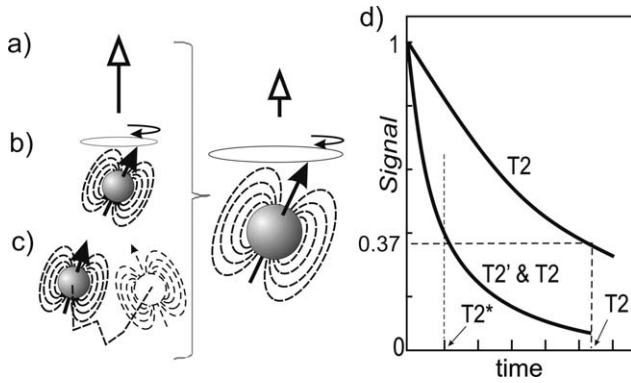


**Figure 5.** Factors that lead to T2\* relaxation. Static field variations in space due to tissue susceptibility variations (a) cause dephasing as discussed in Fig. 4. In addition, random interactions between the magnetic properties of spins themselves (b) and their random motion through regions of different magnetic fields (c) will result in additional loss of signal. Random mechanisms are responsible for decay characterized by T2 while the addition of static field variations leads to faster signal loss as characterized by T2\* (d).

different magnetic fields throughout the tissue. These field variations are categorized into two groups; those that are fixed in time as distinct from those that change with time. Fixed inhomogeneities of the magnetic field can result from the design of the magnet used to form the B<sub>0</sub> field and as such are uninteresting from a biological point of view. However, even with a perfect magnet the tissues can distort the field as a result of their magnetic properties. Changes in tissue magnetic “susceptibility” can generate small field variations on the order of a few parts per million that can vary throughout the tissue (49). Tissues that enhance the field are referred to as paramagnetic, while diamagnetic tissues cause the field to be slightly reduced. As these inhomogeneities are fixed in space and time, the phase angle of magnetization seen in the rotating frame will grow at a constant rate and the resulting signal loss is characterized by a relaxation time T2' (41).

In contrast to field variations that are fixed in time, there are other mechanisms that can generate slowly varying field inhomogeneities with time, as shown in Fig. 5. In addition to the static field variations (Fig. 5a), other magnetic perturbations can arise from the fact that the protons themselves are magnetic and as such can mutually influence each other (Fig. 5b). Furthermore, thermally induced rotations as well as translation of nuclei throughout spatially varying magnetic environments will cause the field that any nucleus experiences to be time-dependent (Fig. 5c). These interactions give rise to time-varying magnetic fields that will generate dephasing and corresponding signal decay. Collectively, these effects give rise to a relaxation mechanism that is often referred to as spin-spin relaxation and characterized by a relaxation time T2 (40). Dephasing from these random time-dependent field variations is not reversible.

Together the static and time-varying field variations combine to cause the signal to decay with a time con-

stant T2\*, which can be shown (41) to be dependent on T2 and T2' as:

$$\frac{1}{T2^*} = \frac{1}{T2'} + \frac{1}{T2}$$

As T2 relaxation arises from only slowly time-varying magnetic interactions, it will always be longer than T2\*, which reflects both static and time-varying effects. It is possible to separate the signal loss from T2' and T2 through the use of a “spin-echo” or “Hahn-echo,” named in honor of Erwin Hahn who first proposed and exploited the concept in 1950 (50). The effect of this pulse sequence is to eliminate the static component of signal loss leaving only the time-varying factors to cause signal decay from spin-spin relaxation characterized by T2.

Relaxation times are key determinates of contrast in MRI and can be used to detect and differentiate a range of pathologies. Early in the history of MRI, a number of investigators showed that neoplasms tended to exhibit longer relaxation times than their corresponding normal host tissues and as such stimulated initial interest in the idea of detecting cancer with NMR (51–57). This initiated a program to catalog the relaxation times of a wide range of biological tissues (1,58), which became one of the main motivations for the development of MRI. A list of key tissues and their corresponding T2 values measured at 1.5 T is given in Table 2 (41), which shows that T2 times are generally on the order of 10–100 msec for many biological tissues of interest. This table shows that there is considerable variation in T2 for these different tissues. Cerebrospinal fluid (CSF) shows the largest value, while blood shows a range of values depending on its oxygenation status. However, it should be noted that these values are quite remarkable when viewed in terms of the loss of synchronization of the magnetization vectors. It suggests that over a period of ≈0.1 seconds (=100 msec), the magnetization vectors throughout the tissue precess in near perfect synchrony. This means that when placed in a static magnetic field of 3 T the magnetization vectors will complete ≈10 million rotations before they begin to show evidence of substantial misalignment.

### SPIN-LATTICE RELAXATION (LONGITUDINAL) TIME

In the preceding section the mechanisms by which spins lose their phase coherence and cause a loss of

Table 2  
T1 and T2 Relaxation Times (1.5 T)

Tissue	T1 (msec) 1.5T	T2 (msec)
Gray matter (41)	950	100
White matter (41)	600	80
Muscle (74)	900	50
Cerebrospinal fluid (CSF) (41)	4500	2200
Fat (41)	250	60
Blood (74)	~1400	~180-250

detected signal characterized by T2 and T2\* were reviewed. However, it is important to note that spin dephasing is a loss of spin orientation after the initial excitation pulse. In this case, the energy that has been deposited by the RF pulse has not been dissipated. However, at longer times this energy will slowly leave the spin system and be dissipated throughout the sample or the "lattice." Consider the situation after the excitation pulse nutates the magnetization into the transverse plane (Fig. 6a). After a few T2 intervals the magnetization is distributed throughout the transverse plane and the signal is lost to detection (Fig. 6b). However, during this same interval the longitudinal magnetization slowly returns to its equilibrium value, as shown in Fig. 6c,d, through a process denoted "T1 relaxation." The time needed to reach  $(1 - e^{-1})$  or 63% of the equilibrium longitudinal magnetization is referred to as the T1 time constant.

T1 values for biological tissues generally increase with applied  $B_0$  field, whereas T2 times are relatively constant. Typical values for relevant biological tissues are shown in Table 2 for a field strength of 1.5 T. It is clear that T1 is generally much longer than T2, although it cannot be claimed in any general sense that T2 and T1 exhibit a strict proportionality. The physical mechanism that mediates T1 relaxation is different from that involved for T2 and once again relates to time-varying changes of magnetic field. However, in the case of T1 the time-varying changes occur at the Larmor frequency, while T2 relaxation is induced by very low frequency field variations. Furthermore, T1 relaxation arises only from components of magnetic field fluctuations in the transverse plane, while T2 relaxation is mediated by fluctuations in all three directions (59). Thus, these two relaxation times report fundamentally different features of molecular dynamics. In subsequent sections the generation of images that reflect these relaxation times through the proper choice of MR pulse sequence parameters will be described. However, it is first necessary to explain how the unique physics of NMR can be used to create images.

### MAGNETIC FIELD GRADIENTS AND MR IMAGE FORMATION

MRI is unique as a medical imaging method in terms of the relation between the detected signals and the final image. As in any digital medical imaging method, the challenge of MRI is to define the intensity of the MRI signal from within an array of pixels corresponding to differing points throughout the anatomy. However, unlike all other medical imaging methods in current use, the signal detecting device (receiver coils) cannot be collimated to restrict the signal to a specific location, as is done in x-ray imaging, CT, ultrasound, or radionuclide imaging. In contrast, the MR signal originates from the entire object rather than a single point within it. Thus, to form MR images it is necessary to determine the location of the signal through some form of encoding scheme. In the case of MRI, this is done through the use of a nonuniform mag-

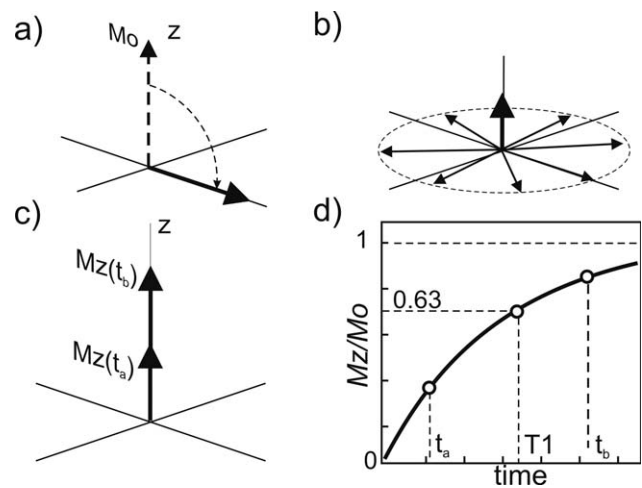


**Figure 6.** Spin-lattice or T1 relaxation. After a 90° excitation, magnetization is nutated into the transverse plane (a) after which it undergoes transverse relaxation and signal loss (b) and a gradual growth of longitudinal (Mz) magnetization with time (c). This results in a curve of Mz with time which is characterized by a relaxation time constant T1, defined as the time to reach 63% of its equilibrium value (d).

netic field which causes the spin location to be encoded in terms of its Larmor frequency. While Paul Lauterbur (28) was among the first to suggest this founding principle of MRI, there is early mention of variants of this idea as it relates to studies of the use of NMR for the detection of spin diffusion (4) and motion (8). Once Lauterbur published his seminal article (28), several independent efforts (29–35) added to a rapidly growing technical literature, which further stimulated the evolution of MRI.

MRI makes extensive use of "magnetic field gradients" and, as such, the meaning of this term should be carefully defined. Great care is used to build the superconducting magnets for MRI so as to achieve a highly homogeneous magnetic field within the magnet bore and are capable of achieving a uniformity better than one part per million field variation over the imaging volume. However, in order to create MR images this field must be distorted in a precise manner through the application of time-dependent magnetic field gradients. This is illustrated in Fig. 7, where an imaging volume is considered. For example, a uniform field shows a uniform color and the sample field vectors throughout the volume are identical in length (Fig. 7a). In contrast, a magnetic field gradient in the Z direction means that the magnitude of the applied magnetic field changes in proportion to the Z location while remaining constant for any point in any X-Y plane (Fig. 7b). In this case, the field on the Y-Z and the X-Z planes is seen to vary only the Z direction, with a gradual shift in color from red to blue. However, for any point in the X-Y plane the field is fixed and seen with a constant color. Similarly, a gradient in X means that the field is proportional only to the X location and otherwise constant in any Z-Y plane (Fig. 7c). Finally, a Y gradient causes the field to change only in the Y direction and is constant within any Z-X

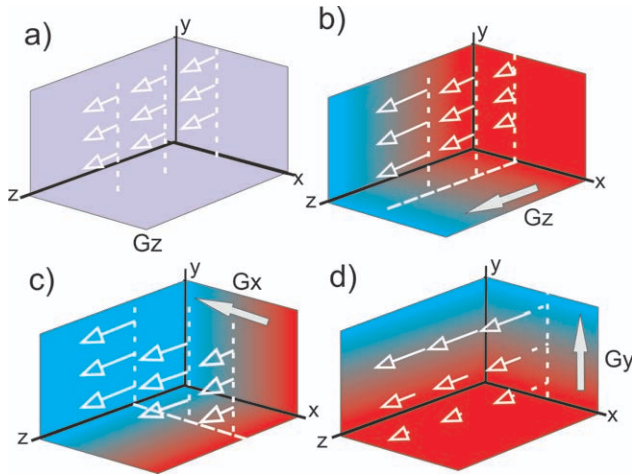


**Figure 7.** A uniform magnetic field (a). Gradients  $G_z$ ,  $G_x$ , and  $G_y$  are the result of additional magnetic field variations shown as color shadings which add to the uniform field, as shown in (b-d) resulting in field variations in the z, x, and y directions, respectively. The gradients add to, or subtract from, the main magnetic field  $B_0$  as a function of position.

plane (Fig. 7d). In addition to these gradients having a direction such as X, Y, or Z, they can also have a magnitude. In this case, the meaning of the magnitude of the gradient refers to the rate with which the field changes per unit distance. A typical gradient can have a value of 10 mT/m, which indicates that the field changes  $10^{-2}$  T for every meter of distance. In comparison to the size of the applied magnetic field ( $\approx 1$  T), these gradients represent very small perturbations ( $\approx 1\%$ ) to the overall field. As these gradients have both magnitude and direction, they can be represented as vectors and as such they can be applied in combination to generate magnetic field gradients in any direction.

**SELECTIVE EXCITATION**

The task of defining the 3D distribution of image brightness throughout an object starts with “selective excitation.” As the name implies, this process creates a slab or section of transverse magnetization that is restricted to a specific plane of prescribed location and thickness. The technique involves the combination of NMR resonance, magnetic field gradients, and a band-limited RF excitation pulse (Fig. 8). Creating an axial image at a specific location shown by the shaded section (Fig. 8a) can be accomplished by applying a magnetic field gradient in the Z direction, which will cause the magnetization to have a Larmor frequency, related to its Z location. Thus, the magnetization that corresponds to the location of the slice of interest will have a continuous range of Larmor frequencies, which span a bandwidth of  $f_1$  to  $f_2$  (Fig. 8b). An RF pulse is then applied that is composed of this band of frequencies (Fig. 8c), which selectively excites magnetization with matching Larmor frequencies. After the RF pulse is completed, the magnetic

field gradient is then removed, which returns the magnetic field to its original homogeneous state. At this point, precessing transverse magnetization has been generated within the desired slice, while the magnetization outside the slice remains aligned with the  $B_0$  field (Fig. 8d). If a suitable receiver coil is placed near the head, an induced signal would be detected, which originates only from the precessing magnetization contained within the selected slice. By controlling the gradient strength and range of frequencies used in the excitation pulse, the width and location of the slice can be controlled. Given that a well-defined slice has now been formed, the task that remains is to define the distribution of magnetization located within this slice.

**MRI SYSTEM, K-SPACE, AND THE IMAGE**

In order to understand how MR images are formed, it is necessary to appreciate the way data are acquired and organized by the MRI system and how the data are reconstructed to form the final image. The features of this process will be explained in two steps. First, the representation of images in Fourier space, also known as “k-space” (60), will be discussed, and the relation between the image and its k-space representation illustrated. Following this, the process by which the MRI system gathers the MRI signals and organizes them into a k-space format will be explained.

**FOURIER TRANSFORM AND THE FORMATION OF IMAGES**

Jean Baptiste Joseph Fourier (1768–1830) was a renowned French mathematician and physicist who

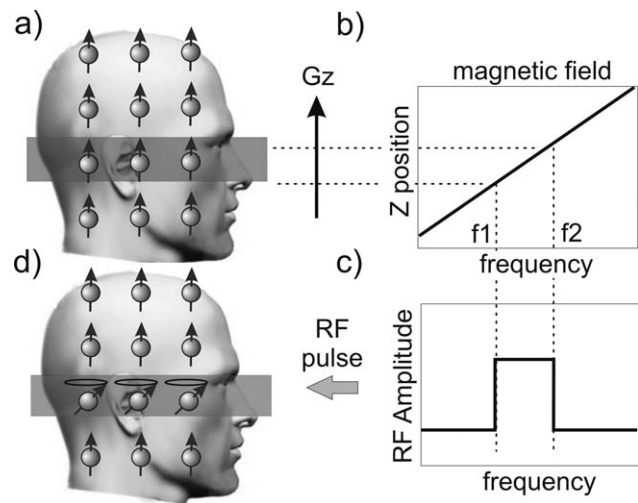


**Figure 8.** The process of selective excitation used to generate transverse magnetization in the shaded section (a). A field gradient  $G_z$  is applied causing a position-dependent field and Larmor frequency. The slice extent corresponds to frequencies from  $f_1$  to  $f_2$  (b). A transient RF magnetic field with frequencies spanning  $f_1$  to  $f_2$  (c) is applied to the tissue to generate transverse magnetization within the desired location (d).

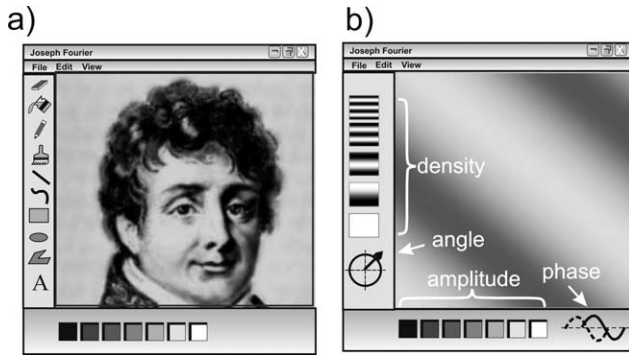


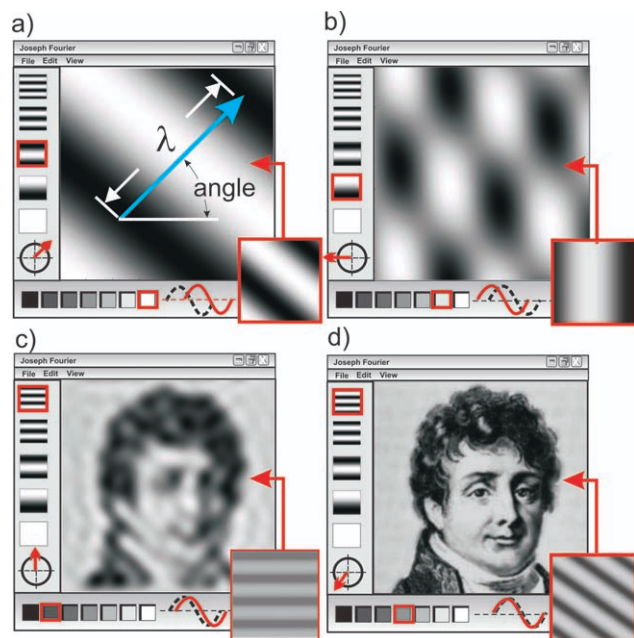
**Figure 9.** Typical tools used to manually sketch an image (a) and the corresponding graphical “tools” used to form MR images (b).

among his many achievements initiated the first studies of the Fourier series, as well as basic studies in heat conduction. He is also generally credited with the first description of the effect of greenhouse gases (61). In addition to its intrinsic mathematical power, the Fourier transform is an extremely useful mathematical tool, which is applied to virtually every branch of quantitative modern science including engineering, physics, and statistics. It is central to the founding principles of MRI.

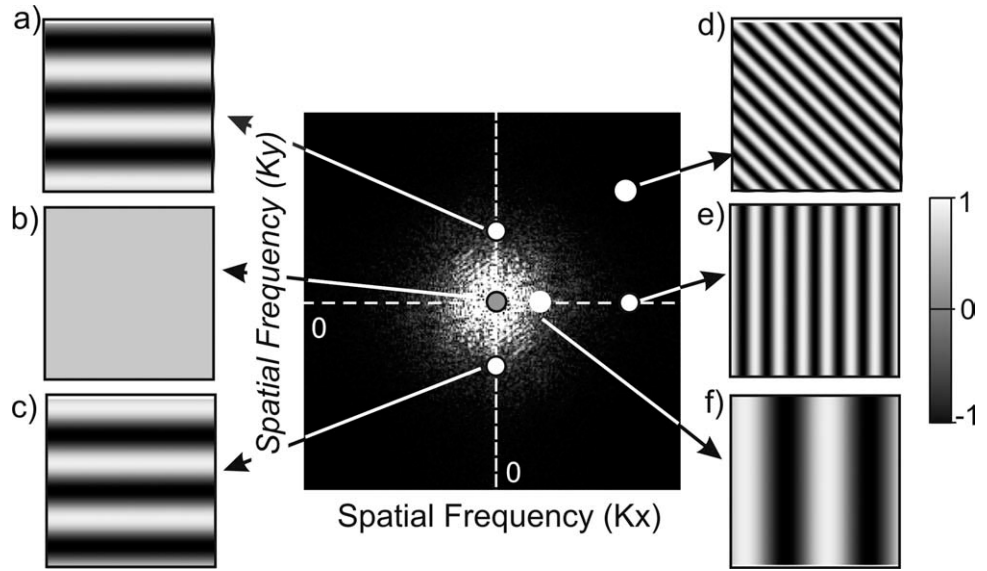
In order to appreciate the Fourier transform it is useful to pause briefly to consider what is meant by an image and how images are traditionally formed. Consider the task of sketching the image of Fourier, as shown in Fig. 9a using a standard computer drawing package. This will generally be equipped with an array of simple tools such as a pencil and paintbrush that are used to draw lines at given locations in the image. By overlaying many of these over the image area, Fourier’s portrait is ultimately formed. While this is a natural and sensible way to imagine drawing an image, this seemingly obvious concept is alien in the MRI domain, where the notion of a “location” is unclear. To appreciate the task of “drawing” in the MRI sense, a new set of tools, as illustrated in Fig. 9b, must be considered. Four basic features are seen that can be combined to form a “stripe” pattern of oscillating positive and negative values represented by white and black gradations across the whole image. These stripe patterns can be altered by adjusting their density, angle, phase, and amplitude as indicated by the controls. Figure 10 illustrates the use of these stripe patterns to form Fourier’s image. An initial stripe pattern must first be selected, which involves the selection of a stripe density, specific angle, phase, and finally the correct amplitude (highlighted red in Fig. 10a). This results in the small inclined stripe pattern enclosed in the red box in the lower right corner of Fig. 10a. This stripe pattern is then applied to occupy the entire image area. The resulting stripe pattern has a wavelength shown by the blue vector of length  $\lambda$  from which the meaning of stripe density as being  $1/\lambda$  can be interpreted. Thus, increasing density means more stripes over the image area. The proper term for this concept is the “spatial frequency” of the stripe

pattern and is measured by the number of gradations per unit length. The blue vector demonstrates the meaning of the angle of the stripe pattern as a measure of the orientation of the stripe pattern. The stripe amplitude is a measure of the contrast of the stripe pattern, which can range from large variations in brightness to an essentially flat gray pattern of no contrast. The concept of phase is more subtle and refers to the symmetry of the stripe pattern relative to the imaging area. More specifically, for any choice of density, amplitude and angle, two sets of similar stripe patterns are combined to form images. The difference between the two patterns is that one of the stripe patterns is shifted by a quarter of a wavelength relative to the other. The measure of phase is a reflection of the relative size of these two stripe patterns. However, for the sake of simplicity, we will continue our discussion by considering only one of these stripe patterns. These four features: amplitude, density, angle and phase, form the set of drawing tools required to form MR images.

To continue with the formation of the image, a second stripe pattern of specific amplitude, spatial frequency, angle, and phase is chosen and is added to the first stripe pattern to form the image seen in Fig. 10b. This second stripe pattern (seen in the lower right corner of Fig. 10b) is seen to have lower amplitude, different phase, a horizontal orientation (angle), and a lower spatial frequency. The result of averaging these two stripe patterns is a patchwork of intensity variations. If 400 stripe patterns of carefully selected combinations of frequency, phase, angle, and amplitude are combined, the formation of a recognizable



**Figure 10.** A stripe pattern (a) of defined density, phase, angle, and amplitude is applied to the image. A second specific stripe pattern is added to form a different image (b). The appearance of the image after the addition of 400 specific stripe patterns (c) and 65,536 stripe patterns (d).



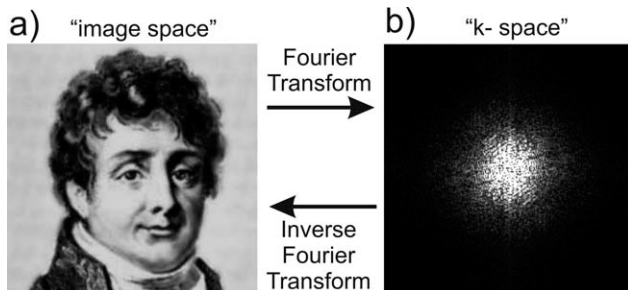
**Figure 11.** Different locations in *k*-space and their corresponding stripe patterns.

image (Fig. 10c) begins to emerge. When the 65,536 ( $256^2$ ) stripe patterns that were defined by the Fourier transform of the original image containing  $256 \times 256$  pixels are used, the original image is recovered with the same resolution (Fig. 10d).

How is the exact combination of frequency, phase, angle, and amplitude identified, such that when their corresponding stripe patterns are combined, the desired image is obtained? The answer to this question is Fourier’s invention—his famous transform. It is a mathematical way to take an image and calculate this array of appropriate stripe patterns. Each image has its corresponding unique array of stripe patterns that can be summarized by represented the data in “*k*-space” (Fig. 11). A point in *k*-space has coordinates *Kx* and *Ky*, which defines its spatial frequency in the X and Y directions. Each location on this image has a brightness that defines the amplitude as discussed in Fig. 10. Horizontal stripe patterns are represented by points along the *Ky* axis, while vertical stripe patterns are represented by points along the *Kx* axis. Oblique stripe patterns are seen as having contributions from both *Kx* and *Ky*. Through these *k*-space representations, the array of spatial frequencies needed to form the desired image can be efficiently summarized. Thus, an image (Fig. 12a) and its *k*-space representation (Fig. 12b) are completely equivalent, with the

Fourier transform of the image used to generate *k*-space, while an inverse Fourier transform of *k*-space results in formation of the original image. If an image is composed of  $256 \times 256$  pixels, its Fourier representation is composed of  $256 \times 256$  stripe patterns.

In Fig. 13, the *k*-space representation of the image of Fourier (Fig. 13a) and the result of adding the stripe patterns from limited regions of *k*-space is shown. If all the stripe patterns were added together, the end result would be the original image seen in Fig. 12a. However, if the summation of stripe patterns of only the central region of *k*-space, restricted to only



**Figure 12.** Jean Baptiste Joseph Fourier (a) and his Fourier transform (b).

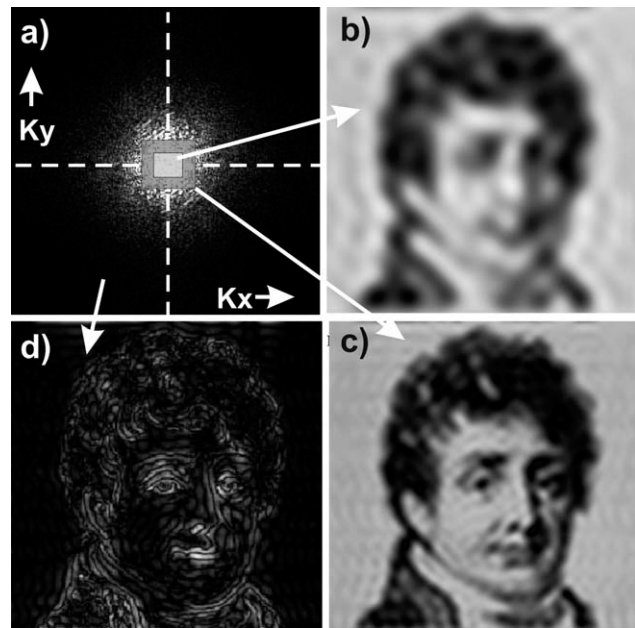


**Figure 13.** The *k*-space representation of the image of Fourier (a) and the inverse Fourier transform from various regions of *k*-space comprising the central 400 spatial frequencies shown from the white region (b), the central 1600 spatial frequencies shown from the gray region (c), and the region outside the gray region (d).

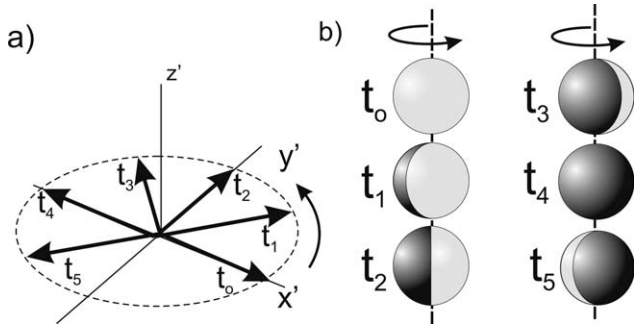


**Figure 14.** Precessing magnetization (a) is represented by a rotating sphere shaded black and white on opposite sides (b). After initial excitation, at time  $t_0$ , the white side of the sphere is aligned with the X axis, which is our point of view. As the magnetization undergoes precession, the appearance of the sphere changes for various times  $t_1$ - $t_5$ .

those within the white zone, the image shown in Fig. 13b would be generated. It is seen as a very blurry and ill-defined representation of the desired image, although it reflects its broad tonal range. If the region of  $k$ -space is increased to the larger (gray) zone, the image seen in Fig. 13c is formed. This shows greater resolution, although it still lacks some detail. The difference between this image and our original image (Fig. 12a) is shown in Fig. 13d and corresponds to the reconstruction from the region of  $k$ -space outside the gray zone. This image shows details near the edges of structures but lacks the correct tonal range. Thus, the periphery of  $k$ -space generates the sharp detail of the image, while the central region carries the broad tonal range of the image (often referred to as the contrast of the image).

In this section the relation between an image and its  $k$ -space representation was discussed and it was recognized that the  $k$ -space domain represents the image data as a multitude of stripe patterns of varying spatial frequency, angle, amplitude, and phase. Next to be addressed is the method by which the MRI system generates these stripe patterns and how the MRI signal defines their correct amplitude and phase, so that when added together they form the desired final image.

**EFFECT OF A MAGNETIC FIELD GRADIENT ON MAGNETIZATION**

Before proceeding any further, it is helpful to change representation of the magnetization discussed in the preceding sections from a rotating vector to something more simple. Specifically, the precessing magnetization will be represented by a sphere instead of a vector, where the sphere precesses on its axis at the Larmor frequency. One side of the sphere will be white, while the opposite side is colored black, as shown in Fig. 14. As the magnetization undergoes precession, the sphere revolves about its axis showing a progressive change from the white to the black side. By looking at the shade of the sphere, the progression of the magnetization phase can be observed as it evolves in varying magnetic environments.

Consider a one-dimensional array of spheres (Fig. 15). After the completion of a selective excitation pulse at time  $t_0$ , the resulting magnetization is seen in the rotating frame as initially aligned. As such, all the spheres are seen in the same orientation, showing the white side of each sphere (Fig. 15a) at time  $t_0$ . An X gradient (Fig. 15c) directed along the array of spheres is now applied. This causes the magnetic field to change over the length of the array (Fig. 15b) such that each sphere will experience a different magnetic field. For example, at the position of sphere *a* the magnetic field deviation is negative and causes the sphere to rotate in a counterclockwise manner in the rotating frame. Spheres toward the right of sphere *a* rotate at a progressively decreasing rate until the central sphere is reached where the magnetic field deviation is zero and the sphere does not rotate. Continuing further to the right, the field gradually increases and results in a clockwise rotation of gradually increasing frequency with position. With increasing time, the orientation of the spheres in the array progresses through a range of patterns for different times  $t_1 \rightarrow t_3$  (Fig. 15a). After a specific period  $t_3$ , the spheres reach a point where neighboring spheres alternate their shade. Thus, the duration of the gradient application, or more generally, the area under the gradient profile, defines the orientation of the spheres in the array as a function of time.

**K-SPACE AND GRADIENT AREA**

The one-dimensional model discussed in the preceding section is easily extended to two dimensions.

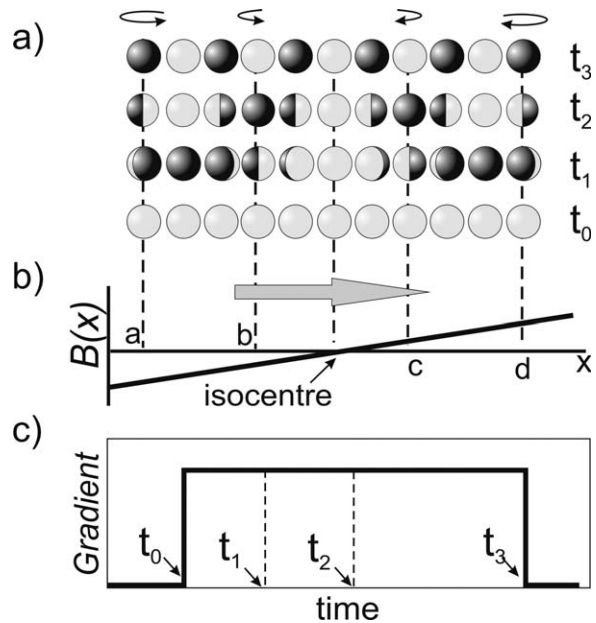


**Figure 15.** A linear array of spheres (a) undergoes precession in a magnetic field gradient (b) for various times. Immediately before the application of the gradient (c) at time  $t_0$ , the field is uniform and the white sides of all the spheres are aligned. The gradient is applied which causes the spheres to precess at varying rates depending on their position within the array. The appearance of the array is shown at times  $t_1$ ,  $t_2$ , and  $t_3$  (a) during the gradient application.

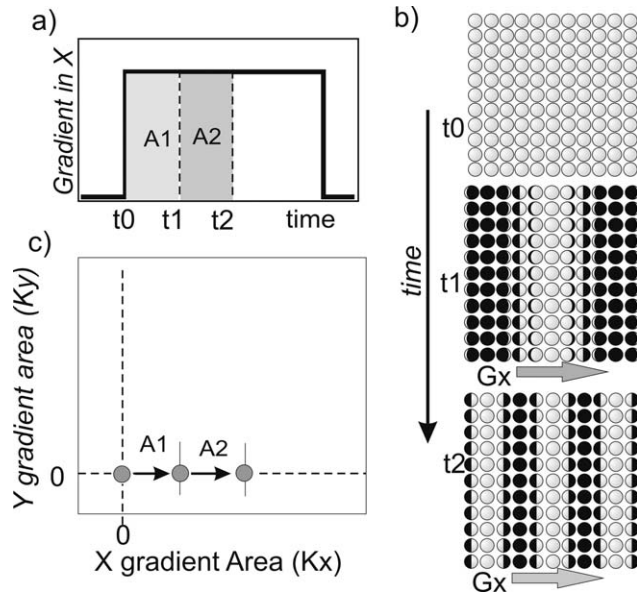


**Figure 16.** A square array of spheres precess (b) in a  $G_x$  gradient for various times (a) during the gradient application. A plot of gradient area for various times (c) is used to characterize the spatial frequency (Kx) of the resulting stripe patterns.

Consider a two-dimensional array of spheres that are exposed to a gradient in the X direction (Fig. 16). Initially the white sides of the spheres are aligned at time  $t_0$ , just prior to the application of the gradient. As the gradient is applied the spheres undergo the precession described in Fig. 15. Their appearance is shown in Fig. 16b at times  $t_1$  and  $t_2$ . The spheres form a vertical stripe pattern with a spatial frequency that depends on the duration of the gradient application. This emergence of a stripe pattern is reminiscent of the Fourier stripe patterns described earlier. Inspecting the sphere array at times  $t_1$  and  $t_2$  shows that the spatial frequency of the array in the X direction increases with time and gradient area. It is possible to create a  $k$ -space representation by constructing a plot with axes that correspond to the area under the X and Y gradients, which are proportional to the spatial frequencies  $K_x$  and  $K_y$ , respectively. In this illustration only a gradient in X is used. Two gradient areas at two different times  $t_1$  and  $t_2$ , corresponding to incremental areas A1 and A2, are shown at their corresponding locations in  $k$ -space (Fig. 16c). The spatial frequency is proportional to the area under the gradient used to form that stripe pattern.

In a similar manner, it follows that using a gradient in the Y direction (Fig. 17) can create horizontally oriented patterns with their corresponding locations in  $k$ -space based on gradient area. Thus, by application of a gradient in either the X or Y directions, stripes in the vertical and horizontal directions, respectively, can be generated. With increasing exposure to these gradients, the spatial frequency of the stripe pattern increases in proportion to the area under the gradient-time plot.

Finally, by using the sequential application of Y and X gradients an oblique stripe pattern can be gener-

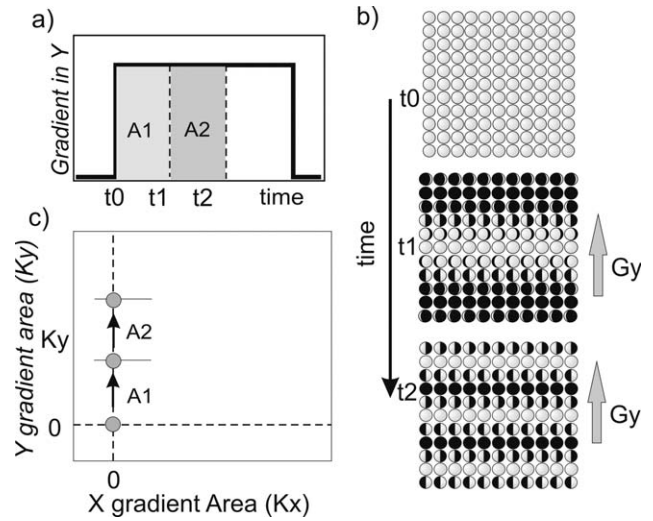


**Figure 17.** A square array of spheres precess (b) in a  $G_y$  gradient for various times (a) during the gradient application. A plot of gradient area for various times (c) is used to characterize the spatial frequency ( $K_y$ ) of the resulting stripe patterns.

ated (Fig. 18). In this case, the Y gradient first generates a horizontal stripe pattern by causing rows of spheres to precess in synchrony. Thereafter, the application of the X gradient causes columns of spheres to undergo rotations, with the final result being an oblique stripe pattern as seen at time  $t_2$ . Referring to the gradient area plot (Fig. 18c), the position in  $k$ -space moves first along the  $K_y$  axis from the origin to a position in proportion to the Y gradient area (A1), after which the X gradient causes the position in  $k$ -space to move parallel to  $K_x$  axis in proportion to the area defined by the X gradient area (A2).

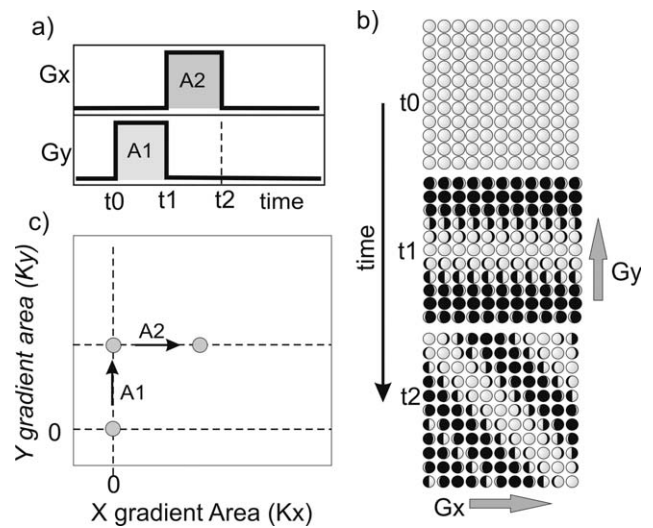


**Figure 18.** A square array of spheres precess (b) in a  $G_y$  gradient followed by a  $G_x$  gradient (a). A plot of gradient area for various times (c) for various times is used to characterize the spatial frequencies  $K_x$  and  $K_y$  of the resulting stripe patterns.

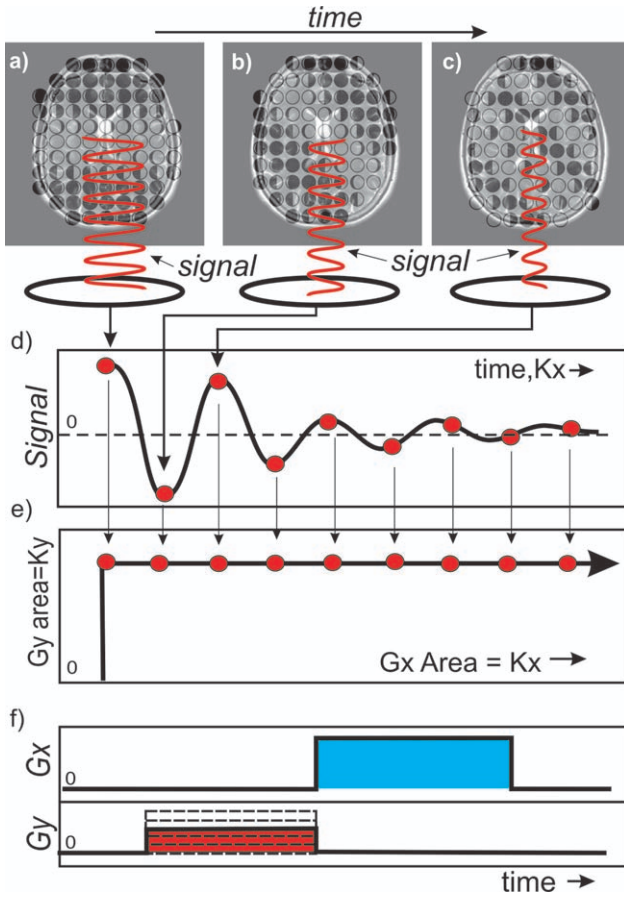


**Figure 19.** The evolution of magnetization (a–c) for various times under the influence of a  $G_x$  gradient after application of a  $G_y$  gradient (f). Location in  $k$ -space (e) is formed by the area swept out by each gradient. Measurements of the time varying NMR signal as detected by the receiver coil (d) defines the amplitude and phase (d) which is applied to the  $k$ -space plot.

**MEASURING THE K-SPACE AMPLITUDE/PHASE**

The application of gradients to create stripe patterns of varying orientation and spatial frequency and their relation to gradient areas have been shown. It should be clear that by applying combinations of X and Y gradients, stripe patterns that correspond to any point in  $k$ -space can be created. The remaining piece of information needed is how the correct amplitude and phase for each spatial frequency to correctly encode the object is determined. This is done by measuring the time-dependent signal arising from the ensemble of rotating magnetization throughout the object during the application of gradients. This is illustrated in Fig. 19, where the object is represented as an axial head image made up of our tiny magnetization spheres. During the application of the gradients (Fig. 19f), the spheres generate the stripe patterns, which evolve with time (Fig. 19a–c). As the stripe patterns evolve, they generate a time-dependent signal, which is detected by the receiver coil (Fig. 19d) and is measured periodically during the application of the  $G_x$  gradient. From this signal the amplitude and

phase of the stripe patterns for a specific line in  $k$ -space (19e) that the gradients define are obtained. Usually, the signals are obtained from two coils placed in an orthogonal arrangement near the patient, as discussed above (Fig. 2b). The signals from these two coils are different due to their relative orientation. The signals can be processed to obtain the desired magnitude and phase for each point in the  $k$ -space plot. In some cases, such as with the use of surface coils, the signal from a single coil can be used to measure phase and magnitude. In this case, a signal processing method is used to effectively simulate the effect of the second coil (62) but has the disadvantage of producing images with slightly worse signal/noise over those produced using two coils. Figure 19f details the gradients used and shows a specific  $G_y$  waveform, which is followed by a fixed  $G_x$  waveform. The MRI signal is sampled during the blue portion of  $G_x$ , while the area under this gradient sweeps out a  $K_x$  trajectory in  $k$ -space. Although only one  $k$ -space line is shown in this illustration, one can increment the  $G_y$  gradient to sweep out a grid of parallel linear trajectories throughout  $k$ -space. It is noteworthy that the gradients illustrated here permit the sampling of  $k$ -space with only the positive values of spatial frequency. As such, this gradient arrangement is not sufficient to explore the full extent of  $k$ -space with both negative and positive spatial frequencies. A simple modification of these gradients that permits sampling of the full extent of  $k$ -space will be introduced in the next section. However, the main message from this discussion is to emphasize that it is possible to migrate through  $k$ -space with the position in  $k$ -space at any moment being defined by the area under the gradients up to that point in time, while the amplitude and phase of the stripe patterns are measured from the MRI signal.

**BASIC MRI PULSE SEQUENCES**

Understanding the  $k$ -space plot enables the formation of a simplified MRI pulse sequence (Fig. 20). The pulse sequence is composed of an RF pulse and  $G_z$  gradient for selective excitation, the MRI signal (shown in gray on the RF line), while the  $G_y$  and  $G_x$  gradient waveforms serve to sample the  $k$ -space features of the

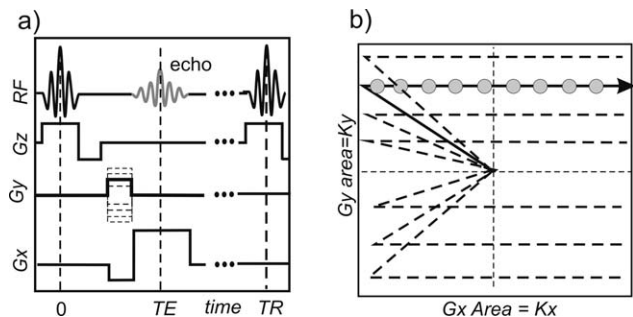


**Figure 20.** A simplified Cartesian gradient recalled-echo pulse sequence (a) and the corresponding trajectory through  $k$ -space (b).  $k$ -space is traversed by incrementing the  $G_y$  gradient prior to the application of a fixed  $G_x$  gradient waveform during which time the echo (shown in gray) is sampled.

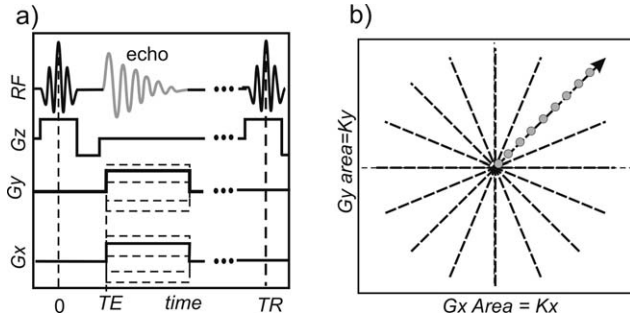


**Figure 21.** A radial gradient recalled-echo pulse sequence (a) and the corresponding radial trajectory through *k*-space (b). *k*-space is traversed by combining Gx and Gy gradients to generate a series of radial trajectories while the echo (shown in gray) is sampled.

object. During the RF pulse, a slice is selected in the presence of a Gz gradient. Then an incremented Gy gradient precedes the Gx gradient. The Gy gradient is often referred to as the “phase encoding” gradient. This gradient has been modified slightly to include negative increments, allowing it to have a negative area and thereby traverse regions with negative values of Ky in the *k*-space plot. The NMR signal, or echo, is sampled during the application of the Gx gradient. The Gx gradient is often referred to as the “readout” gradient and is an example of “frequency encoding.” Once again, note that the addition of a fixed negative lobe immediately prior to the readout gradient allows sampling of regions of *k*-space with negative spatial frequencies. The sampled data are then applied to the corresponding positions in Kx-Ky locations to define the amplitude and phase of the *k*-space data. If Nx by Ny pixels in the image domain are needed, then the pulse sequence requires Ny incremented Gy gradient waveforms after which the echo is sampled Nx times. The time interval between the successive Gy gradients is TR (repetition time). TR is the parameter frequently used to control the T1 weighting of the image. Similarly, the time between the selective excitation pulse and the peak of the MRI signal is the TE (echo time). TE is used to determine the amount of T2\* or T2 weighting in an image. The total time to collect all the *k*-space data for a single slice would be Ny·TR. Typical TR intervals for a “gradient recalled echo” pulse sequence of the type shown in Fig. 20 would be in the range of 10 msec. Because images are routinely acquired with 256 × 256 pixels, the total acquisition time would be 2.56 seconds for a single image with these parameters.

The pulse sequence illustrated in Fig. 20 is an example of a *k*-space trajectory acquired by incrementing Ky lines to form a “Cartesian” sampling scheme. The majority of MRI pulse sequences sample *k*-space using this approach. However, there are advantages to acquiring the *k*-space data using other arrangements of gradients. For example, Fig. 21 illustrates how the Gx and Gy gradients can be applied simultaneously in an incremented fashion. By the proper choice of relative Gx and Gy amplitudes, radial trajectories in *k*-space are possible during which time the MRI signal is sampled and applied to *k*-space. In this case, there is no distinction between the gra-

dients in terms of the order and as such the notion of frequency and phase encoding gradients cannot be applied. This pulse sequence has the advantage that *k*-space is sampled with greater emphasis toward the central regions of *k*-space and less time is spent acquiring the periphery of *k*-space. The net result is that images can be made that require fewer RF repetitions without major effects on image contrast (63,64). Furthermore, the TE interval is measured to the start of the Gx-Gy gradient application and as such can be substantially shorter than that typical of the Cartesian trajectory, where the negative lobe of the readout gradient is required. Variants of this sequence can be used to image tissues with very small T2 values (65).

A third example of a useful *k*-space trajectory is shown in Fig. 22. Once again, this shows the combined use of Gx and Gy while sampling the MRI signal. However, these gradient waveforms provide a spiral trajectory throughout *k*-space. As each spiral can traverse long sections of *k*-space, it is feasible to use each excitation more efficiently, resulting in a further reduction of the number of RF excitations required to fill *k*-space. This can result in a substantial reduction in the time needed to acquire data, and as such is one of the methods of choice for MRI of dynamic processes such as in cardiac imaging (66).

Each of these *k*-space trajectories generate MR images with different imaging properties, contrast, speed, resolution limitations, and artifacts, the details of which are well beyond the scope of this introductory article. A multitude of alternate *k*-space trajectories (67–71) have been proposed in the literature, each of which have special benefits and limitations. However, the main point to be taken from this discussion is that the use of gradient areas to sample *k*-space with the detected MR signal is a flexible process, which allows a very broad array of imaging options and opportunities.

**IMAGE CONTRAST AND PULSE SEQUENCE PARAMETERS**

Given an understanding of how MR pulse sequences are assembled to provide a means of imaging, it is

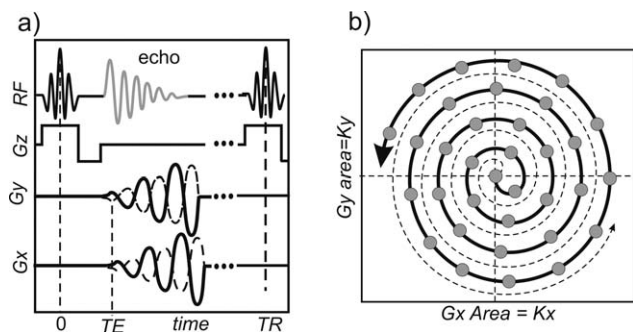


**Figure 22.** A spiral gradient recalled-echo pulse sequence (a) and its trajectory through *k*-space (b). *k*-space is traversed by combining oscillating Gx and Gy gradients that increase with time and are used to generate a series of interleaved spiral trajectories while the echo (shown in gray) is sampled.

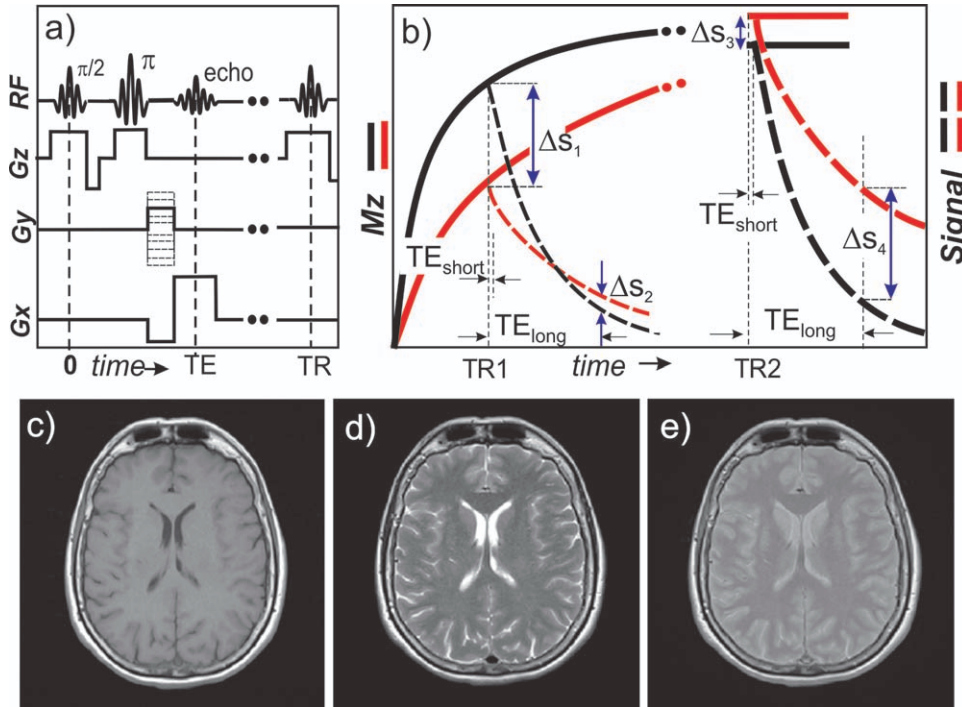


**Figure 23.** The generation of T1- and T2-weighted contrast in spin-echo MRI. A simplified spin-echo pulse sequence (a) is composed of  $90^\circ$  ( $\pi/2$ ) and  $180^\circ$  ( $\pi$ ) selective RF pulses which generate a Hahn echo at time TE. Gradients are applied for a Cartesian  $k$ -space sampling trajectory. The sequence is repeated at intervals of TR seconds. The longitudinal (solid lines) and transverse magnetization (dashed lines) are shown for short (TR1) and long (TR2) repetition times. These are combined with short ( $TE_{\text{short}}$ ) and long ( $TE_{\text{long}}$ ) echo times (b) for two tissues of long T1 and long T2 (red) and short T1 and short T2 (black) relaxation times. The corresponding T1-weighted (c), T2-weighted (d), and proton density-weighted (e) images which result from combinations of varying TR and TE values are shown (see text for more details).

now possible to illustrate how the choice of different timing parameters can be used to generate images with contrast reflecting different relaxation mechanisms. Attention is restricted to the Cartesian spin-echo sequence, which is illustrated in Fig. 23. This sequence is very similar to the one discussed in Fig. 20, but with the inclusion of an additional pulse ( $180^\circ$ ) to form a spin-echo and  $90^\circ$  used for the initial excitation pulse.

Images are described in terms of the various factors that define their contrast. In the simplest situation, MR images can have three kinds of weighting: T1- (Fig. 23c), T2- (Fig. 23d), and proton-density-weighting (Fig. 23e). As the name implies, proton density reflects the variations in the density of protons that are accessible to MRI. Small variations in proton density occur among different soft tissues as seen by the MR system. This is a somewhat unfortunate term in that it does not explicitly reflect gravimetric variations in proton density but rather variations in the abundance of protons available for detection by a specific MRI pulse sequence.

Of greater interest is the creation of T1-weighted images, which are achieved through the timing parameter TR; and T2-weighted images, which are achieved through the timing parameter TE. The mechanism for achieving different weighting is illustrated in Fig. 23b where two tissues, CSF (red curves) and white matter (black curves) with substantially different T1 and T2 values (see Table 2) are considered. The longitudinal magnetization (Mz) for CSF and white

matter as a function of time is plotted in this figure. If a very long time is allowed between sequential RF selective excitation pulses (TR2), the magnetization (Mz) of the red and black tissues converge toward their corresponding equilibrium longitudinal magnetization as reflected through their proton density. If this longitudinal magnetization is then nutated into the transverse plane and a spin-echo generated, each tissue will subsequently decay with their corresponding T2 rates and follow the dashed curves for each tissue. If only a very brief TE interval ( $TE_{\text{short}}$ ) is allowed, the difference in the signals from the two tissues ( $\Delta S_3$ ) will primarily reflect their difference in proton density (Fig. 23e). However, if a long TE interval (shown as  $TE_{\text{long}}$ ) is allowed, the signals from the two tissues will diverge due to their different T2 relaxation rates and generate a T2-weighted image with the red tissue (CSF) being brighter (Fig. 23d). By the proper choice of timing parameters, T2-weighted contrast between the tissues can be achieved shown as  $\Delta S_4$ .

Alternatively, the growth of longitudinal magnetization could be interrupted before either tissue reaches its equilibrium value by using a shorter TR interval (TR1). In this case, the CSF curve would have regained a smaller fraction of its equilibrium magnetization compared to that of white matter due to the longer T1 of CSF. At this point, the longitudinal magnetization of both tissues is converted into transverse magnetization with a spin-echo of short echo time  $TE_{\text{short}}$  to generate

a tissue contrast ( $\Delta S_1$ ). By choosing a short echo time ( $TE_{\text{short}}$ ), any substantial transverse signal decay is prevented, leaving a T1-weighted contrast. In this case, white matter is seen to be brighter than the CSF (Fig. 23c) and is the reverse of that observed on the T2-weighted sequence (Fig. 23d). Finally, if a longer TE period, for this short TR case, was used, the tissue signals would converge until at some point the contrast between the red and black tissues would vanish. A further increase in echo time ( $TE_{\text{long}}$ ) would result in a reversing of the contrast ( $\Delta S_2$ ), with the red tissue being brighter than the black tissue but the signals from both signals being very weak. In this case, the black tissue was biased with a short TR interval, only to have this contrast reduced by a long echo time and an eventual inversion of contrast. This hybrid of T1- and T2-weighting shows little useful contrast and accordingly is not used.

The effect of TR and TE on achieving T1- and T2-weighting has been shown. A similar analysis can be applied when using gradient recalled-echo pulse sequences, although the details are somewhat more complex. In addition to the effect of TR, T1-weighting is also influenced by the choice of the selective excitation flip angle. Furthermore, T2\* relaxation is the salient transverse relaxation factor in gradient recalled pulse sequences, while contrast is modulated by T2 relaxation for spin-echo pulse sequences.

## CONCLUSIONS AND FINAL COMMENTS

In this primer article the basic physics of NMR and the dynamics of proton “spin gymnastics” that work together to make MRI possible has been introduced. While different nuclei can exhibit NMR, protons are the primary means for MRI due to their abundance and large gyromagnetic ratio. Through the use of RF pulses, transverse magnetization can be selectively generated in specific sections of an object in a fashion akin to that of CT scanners. However, MRI offers the option to create sections in orientations that would be impossible for CT systems and offers unique perspectives of anatomy. The magnetic environment at the molecular level mediates different relaxation mechanisms. Transverse relaxation, T2, arises from low temporal frequency changes in the magnetic environment, while T1 relaxation is primarily influenced by temporal magnetic fluctuations at the spin Larmor frequency. Large variations in relaxation times have been found between various normal and diseased tissue. Through the use of pulse sequences with different timing and excitation characteristics, these relaxation time differences can be exploited to great advantage to generate exquisite soft tissue contrast.

The basics of the  $k$ -space representation of an object and its use in MRI has been introduced. Finally, through an analogy with rotating spheres of magnetization, the use of magnetic field gradients to sample the  $k$ -space representation of an object in a general and flexible manner has been shown. The more traditional means of explaining the principles of MRI through the use of frequency and phase-encoding

concepts has been avoided and a more general approach has been adopted through a detailed introduction to  $k$ -space trajectories.

This article is an attempt to present a very basic introduction to the physics of MRI, which hopefully should form the foundation for a more detailed study of the deep MRI literature that has evolved over the past three decades. The interested reader is urged to use these concepts as a transition to the many excellent texts (41,72,73) available, which delve deeper into the subject. Hopefully this article will consolidate some basic concepts to help in exploring the continually expanding technical MRI literature and growing array of clinical applications.

## ACKNOWLEDGMENTS

The authors thank Britton Plewes and Rachel Chan for help with the illustrations in this article and the corresponding lecture “Spin Gymnastics.”

## REFERENCES

1. Bottomley PA, Hardy CJ, Argersinger RE, Allen-Moore G. A review of 1H nuclear magnetic resonance relaxation in pathology: are T1 and T2 diagnostic? *Med Phys* 1987;14:1–37.
2. Haacke EM, Mittal S, Wu Z, Neelavallib J, Chenga Y. Susceptibility-weighted imaging: technical aspects and clinical applications, Part 1. *AJNR Am J Neuroradiol* 2009;26:19–30.
3. Rauscher A, Sedlacik J, Barth M, Mentzel HJ, Reichenbach JR. Magnetic susceptibility-weighted MR phase imaging of the human brain. *AJNR Am J Neuroradiol* 2005;26:736–742.
4. Stejskal E, Tanner J. Spin diffusion measurements: spin-echoes in the presence of time dependent field gradients. *J Chem Phys* 1965;42:288–292.
5. Le Bihan D, Breton E, Lallemand D, Grenier P, Cabanis E, Laval-Jeantet M. MR imaging of intravoxel incoherent motions: application to diffusion and perfusion in neurologic disorders. *Radiology* 1986;161:401–407.
6. Carr H, Purcell E. Effects of diffusion on free water precession in nuclear magnetic resonance experiments. *Phys Rev* 1954;94:630–638.
7. Peters RD, Hinks RS, Henkelman RM. Ex vivo tissue-type independence in proton-resonance frequency shift MR thermometry. *Magn Reson Med* 1998;40:454–459.
8. Hahn EL. Detection of sea water motion by nuclear precession. *J Geophys Res* 1960;65:776–777
9. Gatehouse PD, Keegan J, Crowe LA, et al. Applications of phase-contrast flow and velocity imaging in cardiovascular MRI. *Eur Radiol* 2005;15:2172–2184.
10. Grotenhuis HB, Westenberg JJ, Steendijk P, et al. Validation and reproducibility of aortic pulse wave velocity as assessed with velocity-encoded MRI. *J Magn Reson Imaging* 2009;30:521–526.
11. Walker CL, Foster FS, Plewes DB. Magnetic resonance imaging of ultrasonic fields. *Ultrasound Med Biol* 1998;24:137–142.
12. Kruse SA, Rose GH, Glaser KJ, et al. Magnetic resonance elastography of the brain. *Neuroimage* 2008;39:231–237.
13. Bishop J, Poole G, Leitch M, Plewes DB. Magnetic resonance imaging of shear wave propagation in excised tissue. *J Magn Reson Imaging* 1998;8:1257–1265.
14. Muthupillai R, Lomas DJ, Rossman PJ, Greenleaf JF, Manduca A, Ehman RL. Magnetic resonance elastography by direct visualization of propagating acoustic strain waves. *Science* 1995;269:1854–1857.
15. Williams D, Detrett J, Leigh J, Koretsky A. Magnetic resonance imaging of perfusion using spin inversion of arterial water. *Proc Natl Acad Sci U S A* 1992;89:212–216.
16. Weber MA, Günther M, Lichy MP, et al. Comparison of arterial spin-labeling techniques and dynamic susceptibility-weighted contrast-enhanced MRI in perfusion imaging of normal brain tissue. *Invest Radiol* 2003;38:712–718.

17. Taylor JS, Tofts PS, Port R, et al. MR imaging of tumor microcirculation: promise for the new millennium. *J Magn Reson Imaging* 1999;10:903-907.
18. Scott GC, Joy ML, Armstrong RL, Henkelman RM. Rotating frame RF current density imaging. *Magn Reson Med* 1995;33:355-369.
19. Ogawa S, Lee TM, Nayak AS, Glynn P. Oxygenation-sensitive contrast in magnetic resonance image of rodent brain at high magnetic fields. *Magn Reson Med* 1990;14:68-78.
20. Belliveau JW, Kennedy DN, McKinstry RC, et al. Functional mapping of the human visual cortex by magnetic resonance imaging. *Science* 1991;254:716-719.
21. Bandettini PA, Jesmanowicz A, Wong EC, Hyde JS. Processing strategies for time-course data sets in functional MRI of the human brain. *Magn Reson Med* 1993;30:161-173.
22. Jansen JF, Backes WH, Nicolay K, Kooi ME. 1H MR spectroscopy of the brain: absolute quantification of metabolites. *Radiology* 2006;240:318-322.
23. Jagannathan NR, Kumar M, Seenu V, et al. Evaluation of total choline from in-vivo volume localized proton MR spectroscopy and its response to neoadjuvant chemotherapy in locally advanced breast cancer. *Br J Cancer* 2001;84:1016-1022.
24. Bolan PJ, Meisamy S, Baker EH, et al. In vivo quantification of choline compounds in the breast with 1H MR spectroscopy. *Magn Reson Med* 2003;50:1134-1143.
25. Karczmar GS, Meyerhoff DJ, Boska MD, et al. P-31 spectroscopy study of response of superficial human tumors to therapy. *Radiology* 1991;179:149-153.
26. Formica D, Silvestri S. Biological effects of exposure to magnetic resonance imaging: an overview. *Biomed Eng Online* 2004;3:11.
27. Kanal E, Barkovich AJ, Bell C, et al. ACR guidance document for safe MR practices: 2007. *AJR Am J Roentgenol* 2007;188:1447-1474.
28. Lauterbur PC. Image formation by induced local interactions: examples employing nuclear magnetic resonance. *Nature* 1973;242:190-191.
29. Mansfield P, Grannel PK. NMR "diffraction" in solids. *J Phys C Solid State Phys* 1973;6:L422-426.
30. Garroway AN, Grannel PK, Mansfield P. Image formation in NMR by a selective irradiative process. *J Phys C Solid State Phys* 1974;7:L457.
31. Kumar A, Welti D, Ernst RR. NMR Fourier zeugmatography. *J Magn Reson* 1975;18:69-83.
32. Hinshaw WS, Bottomley PA, Holland GN. Radiographic thin-section image of the human wrist by nuclear magnetic resonance. *Nature* 1977;270:722-723.
33. Damadian R, Goldsmith M, Minkoff L. NMR in cancer: XVI. FONAR image of the live human body. *Physiol Chem Phys* 1977;9:97-100,108.
34. Edelstein WA, Hutchison JMS, Johnson G, Redpath T. Spin warp NMR imaging and applications to human whole-body imaging. *Phys Med Biol* 1980;25:751-756.
35. Clow H, Young IR. Britain's brains produce first NMR scans. *New Scientist* 1978;80:588.
36. Bailes DR, Young IR, Thomas DJ, Straughan K, Bydder GM, Steiner RE. NMR imaging of the brain using spin-echo sequences. *Clin Radiol* 1982;33:395-414.
37. Hawkes RC, Holland GN, Moore WS, Roebuck EJ, Worthington BS. Nuclear magnetic resonance (NMR) tomography of the normal heart. *J Comput Assist Tomogr* 1981;5:605-612.
38. Purcell EM, Torrey HC, Pound RV. Resonance absorption by nuclear magnetic moments in a solid. *Phys Rev* 1946;69:37-38.
39. Bloch F. Nuclear induction. *Phys Rev* 1946;70:460-474.
40. Rahman AU. Nuclear magnetic resonance: basic principles. New York: Springer; 1986.
41. Haacke EM, Brown RW, Thompson MR, Venkatesan R. Magnetic resonance imaging: physical principles and sequence design. New York: (Wiley Liss) John Wiley & Sons; 1999.
42. Levitt M. Spin dynamics: basics of nuclear magnetic resonance. New York: John Wiley & Sons; 2001.
43. Gerlach W, Stern O. Der experimentelle Nachweis der Richtungsquantelung im Magnetfeld. *Zeits Phys* 1922;9:349-355.
44. Dirac PAM. The quantum theory of the electron. *Proc R Soc Lond A* 1928;117:610-624.
45. Uhlenbeck GE, Goudsmit S. Ersetzung der hypothese vom unmechanischen zwang durch eine forderung bezuglich des inneren verhaltens jedes einzelnen elektrons. *Naturwissenschaften* 1925;13:953-954.
46. Goudsmit S. Fifty years of spin: it might as well be spin. *Phys Today* 1976;29:40.
47. Pais A. George Uhlenbeck and the discovery of the electron spin. *Phys Today* 1989;42:34-40.
48. Friedrich B, Herschbach D. Stern and Gerlach: how a bad cigar helped reorient atomic physics. *Phys Today* 2003;56:53-59.
49. Schenk JF. The role of magnetic susceptibility in magnetic resonance imaging: MRI magnetic compatibility of the first and second kinds. *Med Phys* 1996;23:815-850.
50. Hahn EL. Spin echoes. *Phys Rev* 1950;80:580-594.
51. Damadian R. Tumour detection by nuclear magnetic resonance. *Science* 1971;171:1151-1153.
52. Weisman ID, Bennett LH, Maxwell LR Sr, Woods MW, Burk D. Recognition of cancer in vivo by nuclear magnetic resonance. *Science* 1972;178:1288-1290.
53. Hollis DP, Saryan LA, Morris HP. A nuclear magnetic resonance study of water in two Morris hepatomas. *Johns Hopkins Med J* 1972;131:441-444.
54. Hazelwood CF, Chang DC, Medina D, Cleveland G, Nichols BL. Distinction between the preneoplastic and neoplastic state of murine mammary glands. *Proc Natl Acad Sci U S A* 1972;69:1478-1480.
55. Frey HE, Knispel RR, Kruuv J, Sharp AR, Thompson RT, Pintar MM. Proton spin-lattice relaxation studies of nonmalignant tissues of tumorous mice. *Natl Cancer Inst* 1972;49:903-906.
56. Iijima N, Saitoo S, Yoshida Y, Fujii N, Koike T. Spin echo nuclear magnetic resonance in cancerous tissue. *Physiol Chem Phys* 1973;5:431-435.
57. Damadian R, Zaner K, Hor D, DiMaio T, Minkoff L, Goldsmith M. Nuclear magnetic resonance as a new tool in cancer research: human tumors by NMR. *Ann N Y Acad Sci* 1973;222:1048-1076.
58. Cottam GL, Vasek A, Lusted D. Water proton relaxation rates in various tissues. *Res Commun Chem Pathol Pharmacol* 1972;4:495-502.
59. Farrar TC, Becker ED. Pulse and Fourier transform NMR: introduction to theory and methods. New York: Academic Press; 1971. p 48-49.
60. Twieg DB. The k-trajectory formulation of the NMR imaging process with applications in analysis and synthesis of imaging methods. *Med Phys* 1983;10:610-621.
61. Fourier JBJ. Remarques generales sur les temperatures du globe terrestre et des espaces planetaires. *Ann Chim Phys* 1824;XXVII:136-167.
62. Shaw D. Fourier transform N.M.R. spectroscopy, 2nd ed. New York: Elsevier Scientific; 1976. p 136-137.
63. Peters DC, Korosec FR, Grist TM, et al. Undersampled projection reconstruction applied to MR angiography. *Magn Reson Med* 2000;43:91-191.
64. Mistretta CA, Wieben O, Velikina J, et al. Highly constrained backprojection for time-resolved MRI. *Magn Res Med* 2008;55:30-40.
65. Holmes JE, Bydder GM. MR imaging with ultrashort TE (UTE) pulse sequences: Basic principles. *Radiography* 2005;11:163-174.
66. Sachs TS, Meyer CH, Hu BS, Kohli J, Nishimura DG, Macovski A. Real-time motion detection in spiral MRI using navigators. *Magn Reson Med* 1994;32:639-645.
67. Mansfield P. Real-time echo-planar imaging by NMR. *Br Med Bull* 1984;40:187-190.
68. Vahlensieck M, Seelos K, Gieseke J, Reiser M. Turbo(fast) spin echo at 0.5 T: effect of echo distance and echo number on image contrast. *Rofo* 1993;158:260-264.
69. Noll DC. Multishot rosette trajectories for spectrally selective MR imaging. *IEEE Trans Med Imaging* 1997;16:372-377.
70. Feng H, Gu H, Silbersweig D, Stern E, Yang Y. Single-shot MR imaging using trapezoidal-gradient-based Lissajous trajectories. *IEEE Trans Med Imaging* 2003;22:925-932.
71. Ramanna S, Feinberg DA. Single-shot 3D GRASE with cylindrical k-space trajectories. *Magn Reson Med* 2008;60:976-980.
72. Bernstein MA, King KF, Zhou XJ. Handbook of MRI pulse sequences. New York: Elsevier Academic Press; 2004.
73. Stark DD, Bradley WG Jr. Magnetic resonance imaging. St. Louis: C.V. Mosby; 1988.
74. Barth M, Moser E. Proton NMR relaxation times of human blood samples at 1.5 T and implications for functional MRI. *Cell Mol Biol (Noisy-le-grand)* 1997;43:783-791.